

# Pulse shape analysis in segmented detectors as a technique for background reduction in Ge double-beta decay experiments

S. R. Elliott,<sup>a</sup> V. M. Gehman,<sup>a</sup> K. Kazkaz,<sup>b</sup> D-M. Mei,<sup>a</sup> and  
A. R. Young<sup>c</sup>

<sup>a</sup>*Los Alamos National Laboratory, Los Alamos, NM 87545*

<sup>b</sup>*University of Washington, Seattle, WA 98195*

<sup>c</sup>*North Carolina State University, Raleigh, NC 27695*

---

## Abstract

The need to understand and reject backgrounds in Ge-diode detector double-beta decay experiments has given rise to the development of pulse shape analysis in such detectors to discern single-site energy deposits from multiple-site deposits. Here, we extend this analysis to segmented Ge detectors to study the effectiveness of combining segmentation with pulse shape analysis to identify the multiplicity of the energy deposits.

*Key words:*  $^{76}\text{Ge}$ , neutrinoless double-beta decay, Ge detectors, pulse shape analysis, segmentation

*PACS:* 23.40.-s; 29.40.Wk

---

## 1 Introduction

Zero-neutrino, double-beta decay ( $\beta\beta(0\nu)$ ) studies are well motivated on physics grounds and several recent reviews make this case. (See for example Refs. [1][2][3][4].) The process of  $\beta\beta(0\nu)$  may occur in certain even-even nuclei, where  $\beta$  decay is forbidden, but only if the neutrino is a massive Majorana particle. During this process a nucleus will change atomic number by two units while emitting 2 electrons (*e.g.*  $^{76}\text{Ge} \rightarrow ^{76}\text{Se} + 2e^-$ ). Because the rate of this lepton number violating process is proportional to the square of the effective Majorana neutrino mass there is strong current interest in this decay. With the electrons being the only light particles in the final state, the sum of their energies is mono-energetic and therefore a distinct signature for the decay. In any  $\beta\beta(0\nu)$  experiment the peak, if it exists, will be superimposed upon a continuum of background. Present experimental limits indicate the  $\beta\beta(0\nu)$  decay rate would be very low even in the larger mass double beta-decay experiments now being planned making the identification and elimination of background essential.

For the case of  $^{76}\text{Ge}$ , the total energy that the 2 electrons possess is 2.039 MeV. This energy is above most, but not all, the Q-values of naturally occurring radioactive isotopes. The range of the  $\beta\beta(0\nu)$  electrons in a Ge crystal is no more than a couple mm. Therefore, solid state Ge detectors make a high-efficiency experimental apparatus with excellent energy resolution for the study of this decay.

The signature for a  $\beta\beta(0\nu)$  in a Ge detector is a localized deposit of ionization of 2.039 MeV; that is, a single-site event. In contrast,  $\gamma$  rays of a MeV or more tend to multiply scatter as they interact in a solid resulting in a multi-site event. Furthermore, there are potential cosmogenic isotope decays that can populate the  $\beta\beta(0\nu)$  region of interest near 2 MeV including the  $^{68}\text{Ga}$   $\beta^+$  decay and the  $^{60}\text{Co}$   $\gamma$  cascade. All of these background processes tend to produce multi-site energy deposits. This fundamental difference in the energy deposition process creates an opportunity for separating the signal from background.

Ge detectors have been used for several decades in the study of  $\beta\beta(0\nu)$  beginning with the initial work of Ref. [5] culminating with recent state-of-the-art results from the IGEX [6] and Heidelberg-Moscow [7] experiments. In a coaxial Ge detector, the shape of the waveform will primarily depend on the radial distribution of the ionization produced during an event. Both IGEX [8] and Heidelberg-Moscow [9] used pulse shape analysis (PSA) for the latter fractions of their data sets in order to improve their signal to background ratio. Both experiments used large coaxial Ge detectors ( $\approx 2$  kg or 80 mm diameter) resulting in a significant background rejection capability.

In addition to PSA, segmented Ge detectors will also have a capability to identify multiple-site energy deposits. Although this technology has not yet been brought to bear for  $\beta\beta(0\nu)$  it has been used [10][11][12] to ana-

lyze the multiple interactions arising from a  $\gamma$  ray impinging on a detector to "track" the  $\gamma$ -ray path. These  $\gamma$  tracking arrays require very detailed electric field models for each detector in the array[13]. These models are then used to simulate a library of pulses for comparison to the measured pulse. This tracking capability utilizes image-charge formation in adjacent segments to improve event reconstruction and probably provides the highest resolution localization of events in Ge of any technique in use at present.

Recently the Majorana collaboration [14] has proposed to use simple PSA in conjunction with segmentation to further reduce background levels in  $\beta\beta(0\nu)$  without the need for very detailed detector field models. The detector schemes considered for this proposal include segmenting coaxial Ge detectors along either the axial or azimuthal direction. The electronic signals from the various segments would provide information regarding the axial and azimuthal distributions of ionization and therefore should improve on the radial-only information provided by PSA. Although Ge detectors have been produced with a large number of segments (the Gretina detector has 36 segments), the maximum number of segments isn't necessarily the optimum for  $\beta\beta(0\nu)$ . The cost is greater for finer segmentation and the additional detector contacts with their associated electronic components and cables may add to the background.

The purpose of this work is to experimentally measure the effective-

ness of the combination of PSA and segmentation in reducing the background for  $\beta\beta(0\nu)$ . Although we also discuss the reduction of background via a granularity cut (i.e., requiring only one detector in an array observe an energy deposit), we focus on the impact of segmentation. Both segmentation and granularity contribute to an array's self-shielding and hence the identification of single-site energy deposits. The results of this study will aid in the segmentation design to optimally reduce background.

## 2 Experimental Setup

The data for this study were taken using a CLOVER [15] detector. The CLOVER is a close-packed array of four germanium detectors, each 50 mm in diameter and 80 mm long. Each detector is electrically segmented into two parts as shown in Fig. 1. The CLOVER has four high-resolution, cold-FET energy readouts (one for each crystal), and three low-resolution, warm-FET position readouts corresponding to the left two, middle four and right two segments. Coincidences between the energy and position readouts indicate which segment(s) recorded energy depositions.

The major focus of PSA is to distinguish multi-site from single-site energy deposits, and therefore a population of each is required for our study. To this end, we follow the example of Refs. [8] and [9] and use the  $\gamma$ -ray line from  $^{228}\text{Ac}$  at 1588 keV and the double escape peak at 1592 keV derived from the 2614 keV  $\gamma$  ray

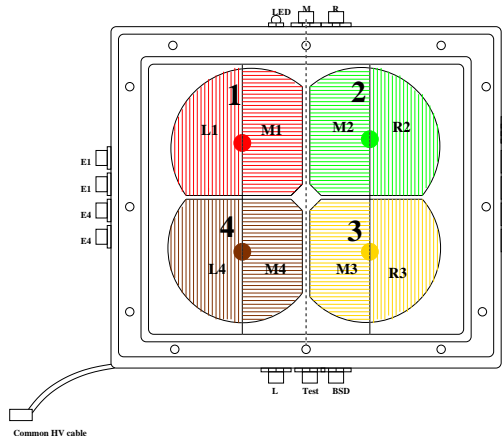


Fig. 1. A schematic sketch of the layout of the Ge detectors in the CLOVER. This figure is a rendition from the owner’s manual.

from  $^{208}\text{Tl}$ . (For reference, the mean free path for a 1.6 (2.6) MeV  $\gamma$  ray in solid Ge is about 4 (5) cm.) Since both of these isotopes are in the decay chain for  $^{232}\text{Th}$ , a single source can be used to obtain both peaks. The 1.6-MeV  $\gamma$  ray from  $^{228}\text{Ac}$  typically interacts about 3 times while depositing its entire energy in a crystal. Hence the full-energy  $\gamma$ -ray peak from  $^{228}\text{Ac}$  consists almost completely of multi-site events. The double escape peak (DEP), conveniently, is completely single-site because it requires the annihilation  $\gamma$  rays from the electron-positron pair production escape the crystal. A Th source spectrum in the energy region near these peaks is shown in Fig. 2. Although both of these processes are required to define the PSA analysis, a nearly pure sample of DEP events can be obtained by requiring a coincident 1592-keV energy deposit in one crystal while simultaneously detecting one of the 511-keV  $\gamma$  rays in a different crystal.

All seven channels from the clover are read out using a pair of X Ray In-

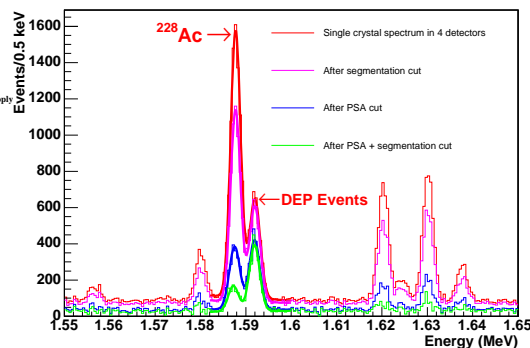


Fig. 2. The energy spectrum of events from a Th source near 1.59 MeV.

strumentation Associates (XIA) [16], Digital Gamma Finder Four Channel (DGF4C) CAMAC modules. These are 14-bit digitizers with a 40 MHz sampling rate. The CAMAC crate is connected to the PCI bus of a Dell Optiplex computer running Windows 2000. The system was controlled using the standard software supplied by XIA. This data acquisition software runs in the IGOR Pro environment [17] and produces binary data files that are read in and analyzed using the ROOT framework.

### 3 Pulse Shape Analysis

Figure 3 shows a current waveform from an event at 1588 keV and therefore most likely a multiple-site energy deposit  $\gamma$ -ray event. Figure 4 shows a waveform from an event at 1592 keV and therefore most likely a single-site energy deposit from a DEP event. The waveforms are clearly different. We analyze the waveforms using the formalism developed by Aalseth [18].

We calculated three different pulse

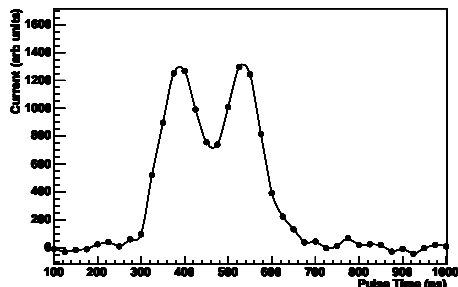


Fig. 3. The current pulse waveform for a pulse near 1588 keV and likely to be an  $^{228}\text{Ac}$   $\gamma$  ray.

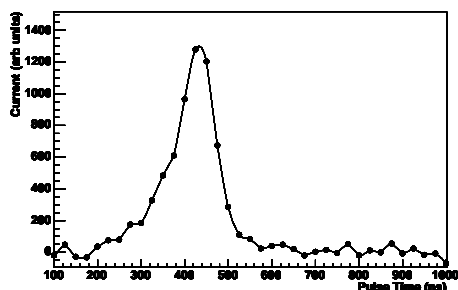


Fig. 4. The current pulse waveform for a pulse near 1592 keV and likely to be a  $^{208}\text{Tl}$  DEP event.

shape parameters (Fig. 5) for each pulse: the width, front-back asymmetry, and a normalized moment. The pulse width is defined by the duration between the times where the charge pulse rises to the baseline plus 10% and 90% of the pulse height. With the pulse mid-point defined as that time half way between the 10% and 90% points, the front-back asymmetry is the difference between the area in the front and back halves of the mid-point of the current pulse divided by the total area of the pulse. Last, the normalized moment parameter is analogous to the moment of inertia if we treat the current pulse as a mass distribution (i.e., it is a sum of the amplitude of the current pulse multiplied by the square of the distance

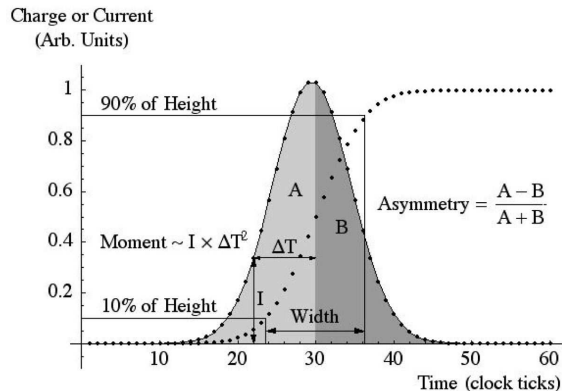


Fig. 5. Cartoon illustrating idealized pulse shape analysis parameters. The monotonically raising curve is a charge pulse, and the shaded-to-zero curve is a current pulse (constructed by differentiating the charge pulse). See text for a detailed discussion of the calculations of the pulse parameters.

from the pulse midpoint). The normalization of the normalized moment parameter ( $I_n$ ) is chosen to minimize any energy dependence. The specific formula is:

$$I_n = 12 \frac{\sum_{i=N_0}^N j_i ((i - N_{mid}) \Delta t)^2}{\sum_{i=N_0}^N j_i \Delta t} \quad (1)$$

where  $j_i$  is the current pulse amplitude at time index  $i$ .  $N$ ,  $N_{mid}$ , and  $N_0$  are the time indices at the pulse onset, midpoint, and end respectively.  $\Delta t$  is the duration of time between clock ticks of the digitizer.

## 4 Data

Once we calculate the three PSA parameters, we form a two-dimensional histogram in the asymmetry and normalized moment parameters. In our pulse shape analysis, we have tended

not to use the pulse width as an analysis parameter because it is largely degenerate between the  $\gamma$ -ray and DEP peak populations. Previous studies have found this parameter useful [18] and we hypothesize that our smaller crystals lead to less sensitivity to this parameter.

We separately fit empirical functions to the two-dimensional histograms of the remaining two parameters for DEP and  $\gamma$ -ray events in a calibration sample of our data. The fit results in two probability distribution functions, one for each class of event (single-site or multi-site) that depend upon the two critical PSA parameters. For a given event, the measured PSA parameters are used to calculate the probabilities that it is associated with a given class. We assigned the event to the single-site or multi-site class for which the probability is higher. This procedure results in accepting 75% of the DEP events but rejects 80% of the  $^{228}\text{Ac}$   $\gamma$ -ray events. The nearby  $\gamma$ -ray peaks that were not used for this calibration have similar rejection results.

One caveat to the comparison between DEP and  $^{228}\text{Ac}$  events is that they have moderately different spatial distributions throughout the detector. The DEP events tend to be somewhat nearer the detector edge because both annihilation  $\gamma$  rays must exit the detector. The mean free path for a 511-keV  $\gamma$  ray in Ge is about 2 cm, which is smaller than the crystal dimensions. Hence the DEP events tend to fall nearer the detector edge where the 511-keV photon has a higher probability to escape. In contrast the

distribution of the  $^{228}\text{Ac}$  events is defined by the 4-cm mean free path of the  $\gamma$  ray to its initial interaction point. In contrast, to DEP events,  $\beta\beta(0\nu)$  events would be uniformly distributed throughout the Ge.

## 5 Simulation

We simulated the distribution of  $^{228}\text{Ac}$   $\gamma$ -ray and  $^{208}\text{Tl}$  DEP events within a Ge crystal of the same dimensions as those composing the CLOVER using GEANT3-GCALOR [19]. We generated  $r$ ,  $\phi$  and  $z$  coordinates for the energy deposits of these events. Figures 6 and 7 show the radial and axial distributions for the simulated DEP events for a source positioned near the front face of the CLOVER.

Pulse Shape Analysis effectively eliminates all multi-hit events in which energy is deposited outside of some "resolution" for identifying radial ionization positions. This effective resolution also depends on the multiplicity of the Compton events, improving as the multiplicity increases (and therefore ensuring the radial ionization distribution exceeds that expected for single-site events). To determine the effective resolution, we establish the resolution which corresponds to rejecting the appropriate number of multi-site events using a Monte-Carlo distribution for the radial separation between the Compton sites. This depends on the type of event (photopeak vs. Compton continuum) both in the predicted spatial distribution for events and in the resolution. For the simulated  $^{228}\text{Ac}$  events, we com-

pared our measured survival probability to the predicted survival as a function of effective separation. From these results (Fig. 8) we estimate the effective  $r$  separation to be 3 mm. That is, an event with multiple energy deposits at radii that differ by more than 3 mm will be interpreted as a multiple-site event. Figures such as 8 and 9 can therefore be used to estimate the survival probability for other segmentation configurations and PSA spatial resolution capabilities.

The measurements indicate that about 3% of the DEP events were rejected due to the segmentation cut. We determined the number of events before and after the cut by fitting to the spectrum. Even so, many of these removed events might originate from  $\gamma$ -ray interactions that form the continuum beneath the DEP peak. If we assume all the removed events are actually DEP events that are excluded because they fall on the border between the segments, however, we can derive an upper estimate for the size of the border. The border is a diameter across the detector face. Therefore, assuming the DEP events uniformly illuminated the front face of the detector, a border width of approximately 1.2 mm would encompass 3% of the DEP events.

To understand the border region better, we scanned the front face of the CLOVER with a collimated  $^{137}\text{Cs}$  source. The collimator was formed by a 2-mm hole through a 4-inch Pb block. We moved this source across the border in steps of 2 mm near the border, and larger steps away from it. We scanned across detector num-

ber 1 moving from the left position region through the border region into the middle position region. The scanning was performed slightly off the diameter to avoid the central core of the detector. The collimator illuminated the detector with a spot size of 3.5 mm diameter. Fig. 10 shows a plot of the average fraction of the energy observed in crystal 1 that is assigned to the left or middle positions for events that populate both segments. Specifically we have plotted  $(E_m - E_l)/(E_m + E_l)$  where  $E_m$  ( $E_l$ ) is the energy in the middle (left) position. We then fit a step function convolved with a Gaussian to these data and took the width of that Gaussian to be the total width corresponding to the finite spot size plus the width of the segmentation border. Since the diameter of the spot was known, we could simply subtract it off to obtain the width of the border region. We calculated this border region width to be 1.9 mm. That is, an event within about 1 mm of the demarcation line will populate both segments. Since this study was done with  $\gamma$  rays, most of the two-segment events are most likely true multi-site events. Therefore this border width estimate is also only an upper limit.

## 6 Analysis

Figure 11 shows the Th source spectrum near the  $^{76}\text{Ge}$  double-beta decay endpoint. Presumably most of the events in this region were from the Compton tail of the  $^{208}\text{Tl}$  2.6-MeV  $\gamma$  ray. Such events are a good model

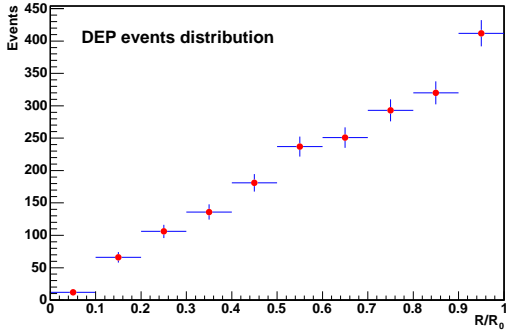


Fig. 6. The radial distribution of simulated DEP events for a source position in front of the CLOVER.  $R_0$  is the radius of the detector (25 mm).

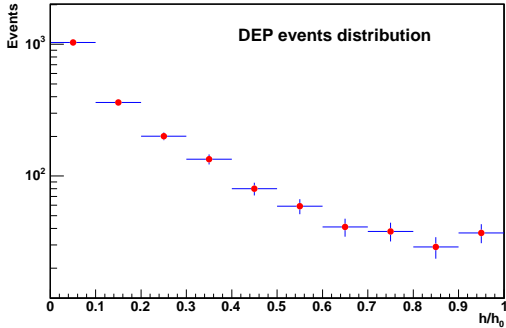


Fig. 7. The axial distribution of simulated DEP events for a source position in front of the CLOVER.  $h_0$  is the total height of the detector (80 mm). The front face of the detector is represented by  $h=0$ .

of background for double-beta decay due to  $\gamma$  rays originating outside the Ge detector. Events within a full energy peak (such as those from  $^{228}\text{Ac}$  at 1.58 MeV) are predominantly multi-site as they are comprised of several  $\gamma$ -ray interactions. The fraction of events in the Compton tail that are single-site, however, is appreciable. Not surprisingly, the rejection of events in this 2.0 - 2.1 MeV window is less than that for the full energy  $\gamma$ -ray peak. Here the survival probability

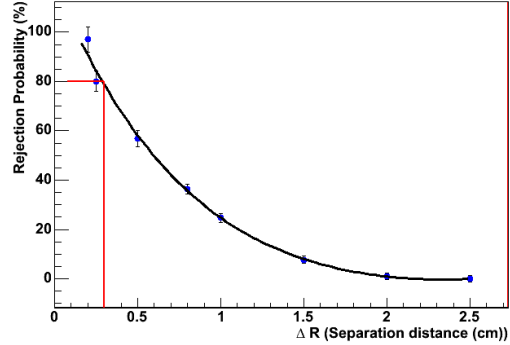


Fig. 8. The fraction of  $\gamma$ -ray events removed as a function of the effective radial separation as predicted by simulation. Our measured PSA rejection probability indicates an effective radial separation of  $\approx 3$  mm for  $^{228}\text{Ac}$  photo-peak events with an average multiplicity of about 3.

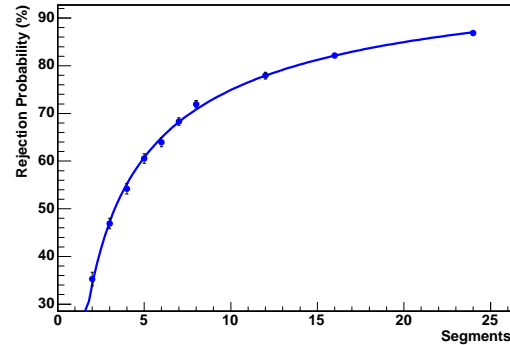


Fig. 9. The fraction of  $\gamma$ -ray events removed as a function of the number of segments as predicted by simulation. The predicted value for 2 segments (35%) agrees with the measured value (34%, see Table 1)

for the two cuts is 30%. In addition, however, a granularity cut is helpful for such Compton scatters. Requiring that only 1 of the 4 detectors has a signal above a 30-keV threshold reduces the rate in this window by a factor of  $1.89 \pm 0.023 \pm 0.09$ , where the first uncertainty is statistical and the second is a systematic



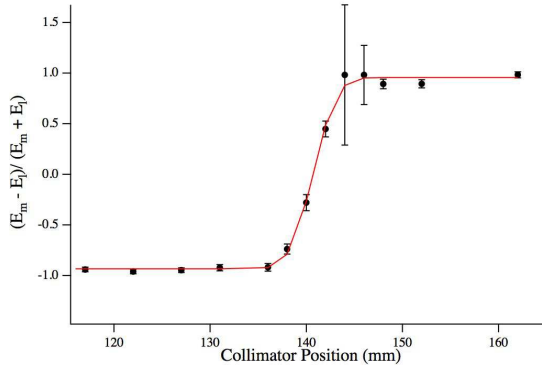


Fig. 10. A measurement of the border width of crystal 1 of the CLOVER. The average fraction of energy assigned to the left and middle positions is plotted as a function of source location. The curve is a fit to the data. See text for discussion of the collimated source. The absolute value of the position scale is arbitrary.

uncertainty estimated by the difference in the results found from different source placements. All our results concerning the segmentation and PSA analyses were calculated on data sets after all events failing the granularity test were removed.

Single-escape peak events (SEP) are necessarily multiple-site energy deposits although typically with fewer interaction points than a 1.59-MeV  $^{228}\text{Ac}$   $\gamma$ -ray event. Thus the survival probabilities for this class of events is between the  $^{228}\text{Ac}$   $\gamma$  ray and the DEP values.

Table 1 summarizes the survival probabilities for the segmentation and PSA cuts and for the combined cuts. The statistical uncertainties are determined from the ratios of events before and after each cut. The systematic uncertainties are estimated by comparing the surviving fractions from three dif-

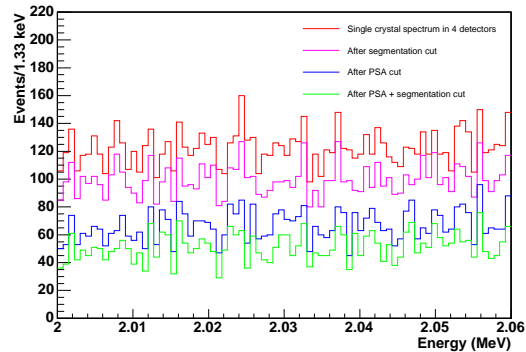


Fig. 11. The energy spectrum of events from a Th source near the  $^{76}\text{Ge}$  double-beta decay endpoint of 2039 keV. The top curve is the raw spectrum, next is the spectrum after the segmentation cut, next is the spectrum after the PSA cut, and the bottom curve is after both segmentation and PSA cuts.

ferent data sets, each with the source at a different location with respect to the CLOVER. The source was located near the center of the front face of the CLOVER, and near 2 sides of the CLOVER.

The PSA survival results are comparable to those found by Aalseth [18] for the  $^{228}\text{Ac}$  1.588-MeV line (26%) and for the DEP line (80%). The survival results are also similar to those of Ref. [20] (20% and 62% respectively).

The data in Fig. 2 and Table 1 show that the product of the measured survival probabilities due to pulse shape analysis ( $P_r = 0.20$ ) and that due to the segmentation cut ( $P_{seg} = 0.66$ ) is greater than the measured survival probability of the joint cut ( $P_{r,seg} = 0.07$ ). This indicates that the two cuts are effective in removing events from separate, but not necessarily exclusive, subsets of the entire data set.

Table 1

A summary of the survival probabilities for each data cut for several processes in the CLOVER. The first uncertainties are statistical and the second are systematic.

Process	Energy	Segmentation	PSA	Seg. and PSA
$^{228}\text{Ac}$ $\gamma$ ray	1.588 MeV	$(66 \pm 1.2 \pm 0.7)\%$	$(20 \pm 0.5 \pm 1.0)\%$	$(7 \pm 0.3 \pm 0.4)\%$
$^{208}\text{Tl}$ DEP	1.592 MeV	$(97 \pm 2.4 \pm 1.2)\%$	$(75 \pm 2.0 \pm 2.1)\%$	$(73 \pm 2.0 \pm 4.0)\%$
$^{208}\text{Tl}$ SEP	2.103 MeV	$(63 \pm 1.4 \pm 1.8)\%$	$(45 \pm 1.1 \pm 4.5)\%$	$(20 \pm 0.7 \pm 2.0)\%$
Compton Continuum	2.0-2.1 MeV	$(81 \pm 1.6 \pm 2.0)\%$	$(43 \pm 0.9 \pm 3.0)\%$	$(30 \pm 0.6 \pm 2.0)\%$
$^{208}\text{Tl}$ $\gamma$ ray	2.614 MeV	$(70 \pm 2.0 \pm 4.1)\%$	$(17 \pm 0.7 \pm 2.2)\%$	$(8 \pm 0.5 \pm 0.4)\%$

These measured values agree with the simulation results plotted in Fig. 12.

By comparing the simulation to the measurements, we can develop insight as to how the survival probabilities change with improvements in the spatial resolutions. Figs. 12 and 13 show that, as one would expect, the joint-cut rejection improves as either the radial resolution improves or the segmentation increases. For the CLOVER, however, the spatial resolutions are rather modest. The segmentation is coarse and the PSA is limited due to this modest segmentation. In more highly segmented detectors, PSA on the induced pulses from multiple segments can greatly improve the spatial resolution. Fig. 13 indicates that if the detector's effective resolution is good in any one dimension, the incremental gain in background rejection by improving the resolution in an orthogonal direction is diminished. In Fig. 13, the joint-cut rejection is shown for a fixed effective radial resolution (3 mm) but as the angular resolution changes. The plot shows that as the angular resolution changes (*i.e.*, the number of azimuthal segments increases from the Clover's current twofold azimuthal segmentation), a value is reached where the

joint-cut survival probability is no longer better than the product of the individual cut survival probabilities.

This situation leads to an optimization opportunity. There is no fundamental need to increase the segmentation beyond the point where  $P_{r,seg} > P_{seg} \times P_r$ . Once this condition is reached, the added spatial resolution has reached a point of diminishing returns with respect to background rejection, but it might be costly to implement. From Fig. 13, this condition is met for an effective radial separation of 3 mm and  $\approx 5$  segments for detectors of the size used here.

## 7 Conclusion

We have measured the rejection of multiple-site energy deposits and the acceptance of single-site energy deposits in a segmented Ge detector by combining pulse-shape analysis with segmentation cuts. We have compared these measurements to simulation to better understand the complementarity of the cuts. Since the two cuts operate on orthogonal coordinates, they tend to remove events from different subsets of the data and there-

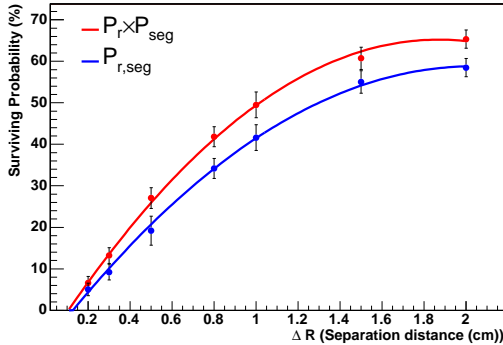


Fig. 12. The joint-cut survival probability ( $P_{r,seg}$ , lower curve) and the product of the individual cut survival probabilities ( $P_r \times P_{seg}$ ) as a function of effective spatial resolution as predicted by simulation for  $^{228}\text{Ac}$   $\gamma$  rays. For both curves, the  $\phi$  survival is determined from a straight-forward segmentation cut. For an effective radial separation of 3 mm, the simulation agrees with the data.

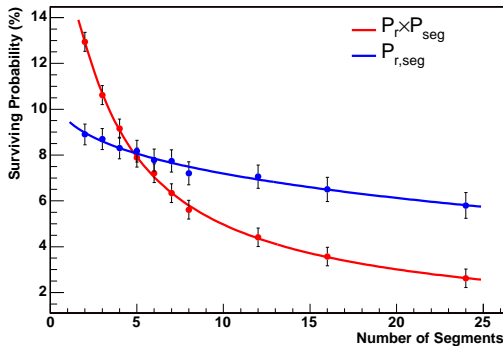


Fig. 13. The joint-cut survival probability ( $P_{r,seg}$ , the mostly higher curve) and the product of the individual cut survival probabilities ( $P_r \times P_{seg}$ ) as a function of effective azimuthal resolution as predicted by simulation for  $^{228}\text{Ac}$   $\gamma$  rays. For both curves, the  $r$  survival is determined by assigning all events with a radial separation greater than 3 mm to be multiple site.

fore the joint action of both tends to be more effective than is predicted from the product of each individual cut. However, as the spatial resolution in one of the dimensions becomes better, the impact of the additional cut is moderated and for very good resolution, the joint cut is not as effective as would be predicted by the product of the individual cuts.

## 8 Acknowledgments

We thank the Majorana collaboration for useful comments and suggestions. In particular, we acknowledge valuable interactions with Craig Aalseth, Reyco Henning, David Radford and Kai Vetter. This work was supported in part by Laboratory Directed Research and Development at LANL.

## References

- [1] Steven R. Elliott and Petr Vogel, *Annu. Rev. Nucl. Part. Sci.* **115**, (2002).
- [2] Steven R. Elliott and Jonathan Engel, *J. Phys. G: Nucl. Part. Phys.* **30**, R183 (2004).
- [3] F.T Avignone III, G.S. King III and Yuri Zdesenko, *New Journal of Physics* (in press 2004).
- [4] A.S. Barabash, *Physics of Atomic Nuclei*, **67**, No. 3, 438 (2004).
- [5] E. Fiorini, *et al.*, *Phys. Lett.* **25B**, 602 (1967).

- [6] C.E. Aalseth, *et al.*, Phys. Rev. **D65** 092007, (2002).
- [7] H.V. Klapdor-Kleingrothaus *et al.*, Eur. Phys. J **A12**, 147 (2001); H.V. Klapdor-Kleingrothaus, A. Dietz, I.V. Krivosheina, and O. Chkvorets, Phys. Lett. **B586**, 198 (2004).
- [8] D. Gonzales *et al.*, Nucl. Instrum. Meth. **A515**, 634 (2003).
- [9] B. Majorovits and H.V. Klapdor-Kleingrothaus, Eur. Phys. J. **A6**, 463 (1999).
- [10] Schmid et al, NIM A, 459 (2001) 565-576
- [11] J. Eberth *et al.* Prog. Part. Nucl. Phys. **46**, 389 (2001); and N. Warr *et al.* Eur. Phys. **A20**, 65 (2004).
- [12] K. Vetter, Eur. Phys. J. **A15**, 265 (2002); Nucl. Phys. **A682**, 286c (2001).
- [13] Th. Kröll, *et al.*, Nucl. Instrum. Meth. **A371**, 489 (1996).
- [14] R. Gaitskell, *et al.*, nucl-ex/0311013 (2003).
- [15] The CLOVER detector is manufactured by Canberra Eurysis, 800 Research Parkway, Meriden CT 06450, USA.
- [16] XRay Instruments Associates, 8450 Central Ave., Newark CA 94560, USA.
- [17] Wavemetrics Inc., PO Box 2088, Lake Oswego, OR 97035, USA.
- [18] Craig Aalseth, "Germanium Spectrometer Pulse-Shape Discrimination for  $^{76}\text{Ge}$  Double-Beta Decay", dissertation Department of Physics and Astrophysics, University of South Carolina (2000).
- [19] R.Brun *et al.*, "GEANT3", CERN DD/EE/84-1 (revised), 1987; C.Zeitnitz *et al.*, Nucl. Instr. and Meth. **A349**, 106 (1994).
- [20] H.V. Klapdor-Kleingrothaus, A. Dietz, I.V. Krivosheina, and O. Chkvorets, Nucl. Instrum. Meth. **A522**, 371 (2004).